BSc Thesis Applied Physics and Applied Mathematics

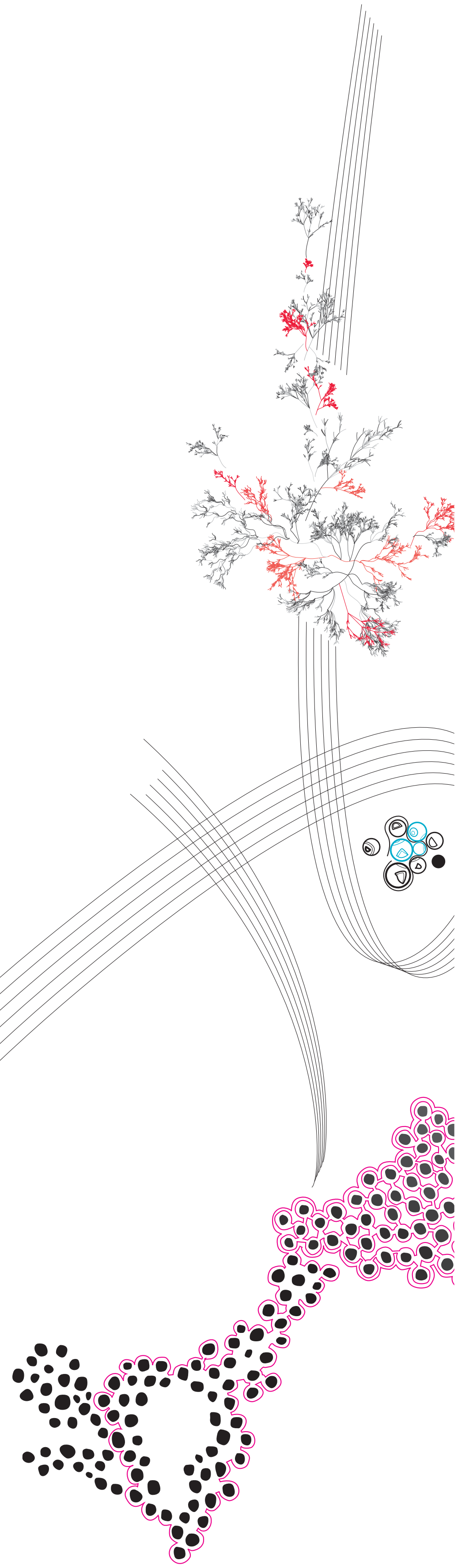

# Modelling and simulation of thermoelectric materials with a superionic phase transition using on-the-fly machine learning force fields

Rick van der Hoeven

Supervisor: M. Bokdam, B.Geurts

July, 2022

Department of Applied Physics
Faculty of Science and Technology

Department of Applied Mathematics
Faculty of Electrical Engineering,
Mathematics and Computer Science

UNIVERSITY OF TWENTE.

## Preface

I want to thank Menno Bokdam and Bernard Geurts for their guidance through my BSc assignment.

# Modelling and simulation of thermoelectric materials with a superionic phase transition using on-the-fly machine learning force fields

Rick van der Hoeven[*]

July, 2022

**Abstract**

Superionic conductors (SIC's) posses liquid like diffusivity in solid state. Materials possessing a superionic phase transition can be researched using first principles calculations. These take long for for bigger system sizes however, and can become impracticable quickly. There is a new method though which can improve on this; on-the-fly machine learning force fields. This method uses first principle calculations to then use these to quicken calculations. It is however not obvious if this method will work; in the superionic phase of the SIC, diffusivity is high and the local environment of atoms varies a lot. In this BSc thesis, we will show that machine learning force fields can indeed model a superionic phase transition for the semiconductor $KAg_3Se_2$. Although the experimental superionic structure is not achieved, we will show that we do indeed observe a superionic phase and a phase transition. Using this, we will convey that we can also get accurate values for diffusion, which are comparable to literature. Finally, we will show that the error of the force field is in reasonable bounds, compared to first principles calculations.

*Keywords*: Machine learning force fields, superionic, thermoelectric

[*] Email: r.vanderhoeven-1@student.utwente.nl

# Contents

# 1 Introduction

## 1.1 Why use thermoelectric materials?

Net zero is a somewhat recent term, referring to the balance between production and removal of greenhouse gasses to and from the atmosphere [7]. This is one of the hot terms currently, with many countries saying they will commit to reaching net zero emissions. With increasing worries concerning climate change, in June 2019 the UK became one of the first major economies to set plans into motion to achieving net zero goals in 2050. Many other countries such as France and Sweden have since followed and put plans into motion to achieve this ambitious goal.

All these claims sound good on paper, but actually reaching these targets is exceptionally challenging. Even the before mentioned UK goals are already quite a bit behind schedule. It is believed that one of the main contributors to reaching net zero is going to be in scientific developments. This means that investing in the right innovative ideas and plans is crucial for developing the right technologies in time so the goals can be reached as planned. This is also quite a challenge however, since there are a lot of different technologies which help reach this goal, such as wind and water turbines, photovoltaics etc.

A good argument as to where most money should go, is to look at where most greenhouse emissions originate from. Around 72% of the global emissions come from the energy production sector [1]. If we look closer at this sector, we can see that almost one third of this energy goes into electricity and heat, which is by far the biggest chunk of the whole energy production. This is also one of the parts where efficiency can most definitely be improved. Waste heat for example is a big problem, which if solved can lead to massive increase in energy efficiency and hence also lead to reduction in emissions.

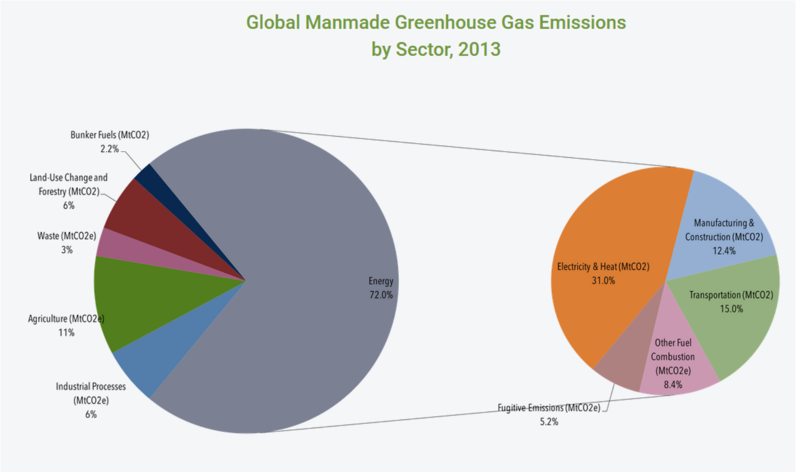

FIGURE 1: Pie chart showing global manmade greenhouse gas emissions per sector in 2013 [1]

Where does this waste heat come from? It is reported that about 20% of the total energy conversion is effective, meaning that 80% is converted into environmental or waste heat [4]. From this 80 %, about 44% comes from the industrial sector, and 36% originate from residential and commercial sectors. So it seems that targeting these sectors with funding and attention could be one of the key ingredients to achieving the net zero goals.

One technology that could help solve the waste heat problem, is in thermoelectrics. As the name suggests, thermoelectric materials are materials which can convert heat into electricity by applying a temperature gradient to the material. These materials can hence convert waste heat directly into electrical energy, and also provide full cooling and heating technology without the need of moving parts or refrigerants. The part of not needing refrigerants is appealing, since these are also notorious for being greenhouse gasses.

Thermoelectric materials have already been known for about a century, yet they are not very much applied yet. Apart from niche sectors such as the aerospace sector, the current state of the technology leaves a lot to be desired for more widescale application. One of the reasons for this is the low efficiency of current materials. Another one of the reasons for the lack of application is the sustainability of the materials. Hence, current research in thermoelectrics is being done in making sustainable materials with high performance characteristics. This may seem like big hurdles, but one must be reminded that the possible gain of this technology is also significant. It is hence of great advantage for countries aiming for net zero to invest in developing these materials.

While there are a lot of known thermoelectric materials, this report will look closer into a specific type of these materials; thermoelectric materials with a superionic phase transition, also called superionic conductors (SIC's). Having a superionic phase transition means having a sudden sharp increase in diffusion of ions within the material at a certain temperature. This diffusion is often comparable to that of a liquid at room temperature [source], while the rest of the material stays solid. As we will see later, these SIC's have very desirable properties for thermoelectric generators, such as very low thermal conductivity and high ionic conductivity. This combination would help to retain a given temperature gradient intact while 'harvesting' electrical power from it - this is potentially a breakthrough.

## 1.2 The newcomer; Machine Learning Force Fields

The mechanism behind this superionic phase transition is however still poorly understood. Simulations trying to uncover the phenomenon often would take extremely long, and it would become very impracticable. A new method has shown up recently however, which could help with the computation cost; so-called machine learning force fields (MLFF). As we will see later, this method makes calculations orders of magnitude faster than previous methods, which enables the possibility of simulating the superionic transition at smaller time scales.

There is however no guarantee that this method is accurate, or will even work for that matter. This is because this method relies on the surroundings of an atom not changing 'too' much, because this can blow op the system size. Since superionic materials contain a highly diffusive layer, it is entirely possible that there are too many 'different' structures to learn and hence the method will not be practicable anymore.

This is exactly the main aim of this bachelor thesis; to verify whether the MLFF method can reproduce the superionic phase transition in the semiconductor $KAg_3Se_2$. If so, then another question becomes how accurate it is, and how well properties like diffusivity compare to literature.

## 1.3 A 2D Superionic Conductor

The material of interest is the semiconductor $KAg_3Se_2$. This is not just a semiconductor however; it has been reported [11] that this material has a superionic phase. At around 675 K, the low-temperature $\beta$-phase transforms into the superionic $\alpha$-phase through a type I superionic phase transition (see section 2.1). At this temperature, the silver ions start to hop between sites, creating a highly diffusive layer between immobile selenium layers. The potassium-selenium structure prohibits the silver atoms from diffusing between different

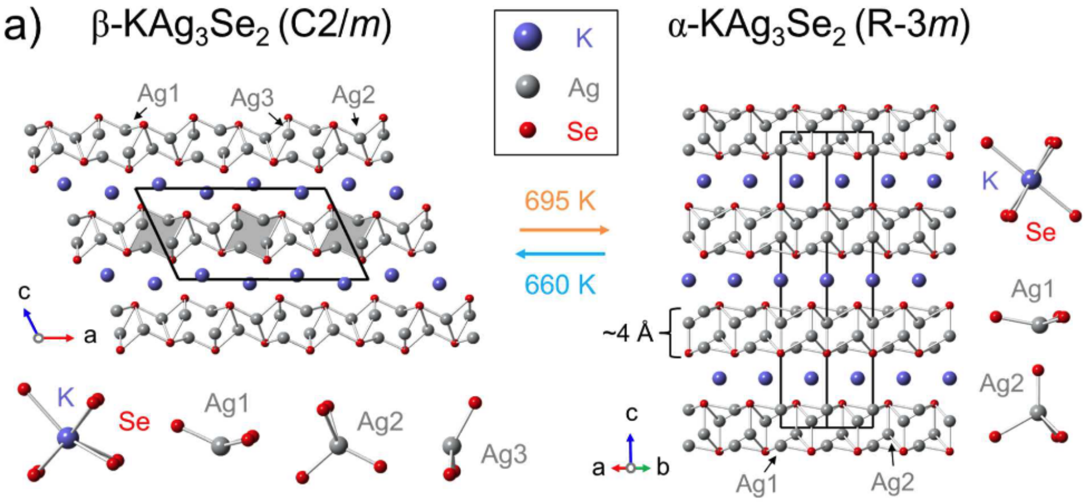

FIGURE 2: Different phases of $KAg_3Se_2$. On the left, the low-temperature $\beta$-phase is shown, and on the right the superionic $\alpha$-phase is shown [12].

layers, creating a two dimensional superionic conductor. The fact that the diffusion is two dimensional can be of interest in application to for example batteries. Using a 2D material in batteries can help a multitude of problems that 3D materials face. They do this by for example increasing thermal stability, improve ion flux through the different interfaces and protect the materials from pulverization [14]. They also for example have a lot more active sites [13].

The transition between the two phases is quite complex, or maybe even better said; the unit cell changes quite a bit from structure. The unit cell transforms from a wide to a long unit cell, as can be seen in figure 2. Not only does the lattice parameter $c$ almost triple, but the lattice parameter $a$ also gets divided by four. These are not the only changes however; also the angle between these parameters change significantly. All of this makes the transition quite a complex one. The exact values are given in the table below.

| Phase | a (Å) | b (Å) | c (Å) | $\alpha$(°) | $\beta$(°) | $\gamma$(°) |
|---|---|---|---|---|---|---|
| $\beta$ | 16.163 | 4.39149 | 8.7768 | 90 | 115.546 | 90 |
| $\alpha$ | 4.5638 | 4.5638 | 25.4109 | 90 | 90 | 120 |

TABLE 1: Table showing the different unit cell lattice parameters and angles for different phases of $KAg_3Se_2$ [12].

As we will show in this report, while we do not see this exact phase transition, we do see an phase transition. From this, we can deduce properties of $KAg_3Se_2$ and compare them with literature.

The organization of this report is as follows. In section 2, we will go over the basic principle behind superionic conductors, and introduce the machine learning force fields theory. Then in section 3, the on-the-fly method will be introduced, along with the various settings and the numerous procedures for all experiments will be explained. In section 4, we will go over all the results one by one and discuss them aswell. Finally, we will conclude in section 5 and give a short outlook in section 6.

# 2 Theory

## 2.1 Superionic conductors

Superionic conductors (SIC's) are solid state systems (crystals, semiconductors, ect) which have ions showing very high diffusivity at a certain temperature. In the high conductivity regime, measurements for the diffusion coefficient $D$ usually yields values of around $D = 10^{-5}\text{cm}^2\text{s}^{-1}$, which is comparable to the diffusivity of water at room temperature. This makes these types of materials unique, in the sense that they are solids possessing liquid like behaviour. What is furthermore interesting is that if only one type of ion is the charge carrier, an simple estimate of the charge carrier concentration $n$ can be obtained which yields $n$ $10^{22}$ carriers/cm$^3$. This is almost a whole sublattice of the solid. From this result it is believed that a whole ion sublattice moves as some sort of liquid, going from site to site which is provided by the solid sublattice.

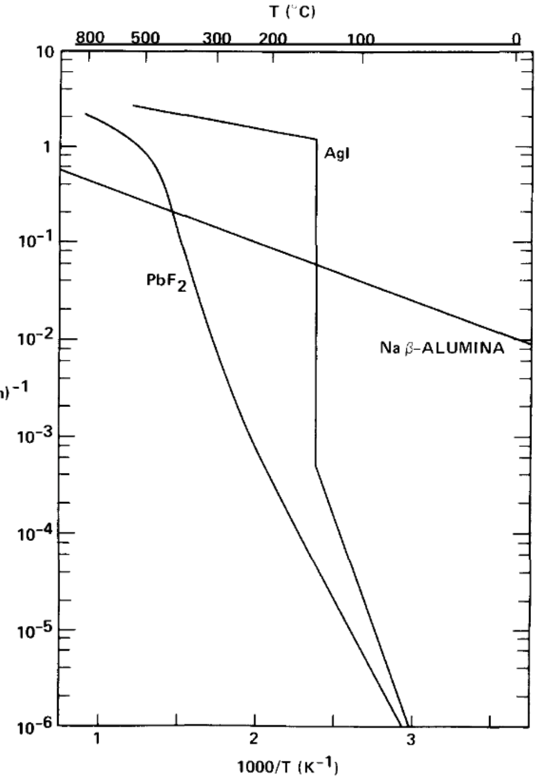

FIGURE 3: Graph showing the different types of superionic conductors. Here, AgI is a type I SIC, PbF$_2$ is a type II SIC and Na$\beta$ − ALUMINA is a type III SIC [6].

An important aspect of these SIC's is that they get to the superionic phase through a well defined phase transition. If the material is heated from low to high temperature, the type of transition can be characterised into three types. Firstly there are type I superionic conductors, whose phase transition are characterised by a very sharp change in conductivity, changing orders of magnitude in a small range around the transition temperature $T_c$. Secondly there are type II SIC's, which have a sharp but way more smooth transition around $T_c$, which can be seen as going from an insulating to a conducting state. Lastly there are type III superionic conductors, which have an exponential growth of conductivity. A graphical representation of the three types can be seen in figure 3. In this research, since the SIC researched is of type I (see section 1.3), we will only discuss this type in more detail.

As said before, type I superionic conductors are defined by a sharp increase in conductivity around the transition temperature. For many of these materials, around $T_c$ a rearrangement of both the immobile lattice and a disordering of the conducting sublattice occur. This makes it relatively more complicated than if only one of the layers were to change, since now there are two layers which change instead of one. This gives an extra degree of freedom, which is believed to be responsible for the very sharp increase in conductivity around $T_c$.

## 2.2 Machine learning force fields

### 2.2.1 The aim of Machine Learning Force Fields

The goal of machine learning force fields is to describe the potential energy surface (PES) of a system. The PES ($\mathrm{U}(\{\mathbf{R}_i\})$) is described in terms of atomic coordinates $\{\mathbf{R}_i\}$ in the crystal, and is hence dependent on them. To represent the PES, a variant of the Gaussian approximation potential (GAP) [3] is used. Following this method, the objective is to find:

$$U = \sum_{i=1}^{N_a} U_i, \tag{1}$$

where $U$ is the potential energy, $N_a$ is the number of atoms and $U_i$ is the local atomic potential energy assigned to atom $i$. The idea is that if we assume the local energy $U_i$ to be fully defined by its environment, we can look at the local environment within a certain cutoff radius $R_{cut}$ of each atom individually and calculate the local energy and then sum over these energies. It is assumed that everything outside this cutoff radius does not contribute much to the local energy.

### 2.2.2 Descriptors

For this to work we need a way to describe the environment of an atom. To this end, the local environment is mapped onto a set of so called descriptors. Descriptors are feature vectors which describe the local environment around an atom within the cutoff radius. This is done by using the distribution of other atoms around atom $i$. The distribution is given as a probability distribution $\rho_i(\mathbf{r})$, which describes the probability to find another atom $j$ at position $\mathbf{r}$ [9]:

$$\rho_i(\mathbf{r}) = \sum_{i}^{N_a} f_{cut}(r_{ij}) g(\mathbf{r} - \mathbf{r}_{ij}), \tag{2}$$

where $f_{cut}(r_{ij})$ is a cutoff function which smoothly removes the information outside the cutoff radius $R_{cut}$. The position of atom $i$ is given $\mathbf{r}_i$, and hence we also have the difference vector $r_{ij} = |\mathbf{r}_{ij}| = |\mathbf{r}_j - \mathbf{r}_i|$. Lastly, $g(\mathbf{r})$ is the delta function. A different function is used however to approximate the delta function, since the delta function is impractical on the computer. The approach is called the SOAP [2] method and replaces the delta by a Gaussian function:

$$g(\mathbf{r}) = \frac{1}{\sqrt{2\sigma_{atom}\pi}} \exp -\frac{|\mathbf{r}|^2}{2\sigma_{atom}^2} \tag{3}$$

One of the upsides to this is that this mimics the influence of temperature on the system, since it is a smeared out version of the delta function and hence smears out the positions of the atoms. We now have that the local potential energy of an atom is dependent on the probability distribution, i.e $U_i = F[\rho_i(\mathbf{r})]$. The simplest procedure now would be to develop $\rho_i(\mathbf{r})$ into a finite basis set and express $F$ as a function of the coefficients. The problem here however is that $\rho_i(\mathbf{r})$ does not have rotational invariance, which is very impractical since this would mean that if we rotate our system, we would get a different energy. So even though the system is the same for the atom we are looking at, we have to treat it as a different system. This means that our machine has more unnecessary learning work to do.

To overcome this problem, intermediate functions are introduced which depend on $\rho_i(\mathbf{r})$. The aim is to let these functions be invariant under rotation, translation, and permutation of atoms. A good choice of descriptor is the so called radial distribution function, which is given by [9]:

$$\rho_i^{(2)}(r) = \frac{1}{4\pi}\int \rho_i(r\hat{\mathbf{r}})d\hat{\mathbf{r}}, \tag{4}$$

where $\hat{\mathbf{r}}$ denotes the unit vector of $\mathbf{r}$. This function calculates the distance between atom pairs from atom i to another atom within $R_{cut}$. If we were to use only this function as descriptor however, we would lack angular information. This leads to some configurations being seen as the same, which would lead to the same local potential energy. To combat this, another descriptor is introduced which is called the angular distribution function. This function describes the probability to find an atom $j$ at a distance $r$ from atom $i$, and another atom $k$ at a distance $s$, with an angle $\theta = \angle kij$. The probability is given by [9]:

$$\rho_i^{(3)}(r,s,\theta) = \iint \delta(\hat{\mathbf{r}}\cdot\hat{\mathbf{s}} - \cos\theta)\rho_i(r\hat{\mathbf{r}})\rho_i^*(s\hat{\mathbf{s}})d\hat{\mathbf{r}}d\hat{\mathbf{s}}. \tag{5}$$

These two descriptors together are used to describe the local environment of an atom.

It is useful to expand equation 2 into basis functions:

$$\rho_i(\mathbf{r}) = \sum_{l=1}^{L_{\max}}\sum_{m=-l}^{l}\sum_{n=1}^{N_R^l} c_{nlm}^i \chi_{nl}(r) Y_{lm}(\hat{\mathbf{r}}), \tag{6}$$

where $\chi_{nl}$ denote radial basis functions, in our case Spherical Bessel functions, $Y_{lm}$ are spherical harmonics and $c_{nlm}^i$ are expansion coefficients. Combining equations 4, 5 and 6 we obtain:

$$\rho_i^{(2)}(r) = \frac{1}{\sqrt{4\pi}}\sum_{n=1}^{N_R^0} c_n^i \chi_{nl}(r), \tag{7}$$

$$c_n^i = c_{n00}^i \tag{8}$$

$$\rho_i^{(3)}(r,s,\theta) = \sum_{l=1}^{i}\sum_{n=1}^{L_{\max}}\sum_{v=1}^{N_R^l}\sqrt{\frac{2l+1}{2}}p_{nvl}^i\chi_{nl}(r)\chi_{\nu l}(s)P_l(\cos\theta) \tag{9}$$

$$p_{nvl}^i = \sqrt{\frac{8\pi^2}{2l+1}}\sum_{m=-l}^{l} c_{nlm}^i c_{vlm}^{i*}, \tag{10}$$

where $P_l$ is a Legendre polynomial of order $l$. While this might seemingly come out of nowhere, the coefficients used to fill the descriptors in the next chapter are actually the Fourier coefficients $c_n^i$ and $p_{nvl}^i$ for the radial and angular descriptors respectively.

### 2.2.3 Kernel Regression

In the previous chapter, we have assumed that the local potential energy is a functional of the local environment. Using the descriptors found in the previous chapter, we can now write this as $U_i = F\left[\rho_i^{(2)}, \rho_i^{(3)}\right]$. So the task which is left now is to find a suitable functional $F$. The way this is done in the GAP method is by using a so called kernel-regression method. We write the functional as a sum of weights multiplied by a kernel $K$ [10]:

$$U_i = F\left[\rho_i^{(2)}, \rho_i^{(3)}\right] = \sum_{i_B=1}^{N_B} w_{i_B} K(\mathbf{X}_i, \mathbf{X}_{i_B}). \tag{11}$$

In this equation, $i_B$ is a local reference structure, $\{w_{i_B} | i_B = 1, ..., N_B\}$ is the set of linear fitting coefficients, $\mathbf{X}_{i_B}$ is a reference configuration in the descriptor space, and $\mathbf{X}_i$ is the local configuration of interest in the descriptor space. These $\mathbf{X}_i$ and $\mathbf{X}_{i_B}$ contain the coefficients $c_n^i$ and $p_{nvl}^i$ for a specific or reference configuration, respectively. Lastly, $K$ is called a kernel function, and this function measures the similarity between the two input vectors. The value goes to zero for low similarity, and to one if high similarity is found. The kernel used in this research is given by [9]:

$$K\left(\mathbf{X}_i, \mathbf{X}_{i_B}\right) = \beta^{(2)}\left(\mathbf{X}_i^{(2)} \cdot \mathbf{X}_{i_B}^{(2)}\right) + \beta^{(3)}\left(\hat{\mathbf{X}}_i^{(3)} \cdot \hat{\mathbf{X}}_{i_B}^{(3)}\right)^{\zeta^{(3)}}, \tag{12}$$

where the (2) in the power stands for the vectors $\mathbf{X}_i$ containing $c_n^i$, and the (3) in a power stands for vectors containing $p_{nvl}^i$. Furthermore, $\hat{\mathbf{X}}_i^{(3)}$ stands for a normalised version of $\mathbf{X}_i^3$. Lastly, $\beta^{(2)}$ and $\beta^{(3)}$ are weighting parameters, and $\zeta^3$ is a parameter which controls the sharpness of $K$.

### 2.2.4 Fitting

Using equation 11, we can describe the energies, forces and stress tensor (EFS's) as:

$$\boldsymbol{y} = \boldsymbol{\phi}\boldsymbol{w}, \tag{13}$$

where $\boldsymbol{w} = \{w_{iB}\}$ is the set of weights and $\boldsymbol{\phi}$ is a matrix which contains $K\left(\mathbf{X}_i \mathbf{X}_{i_B}\right)$ and its derivatives. Then $\boldsymbol{y}$ contains the EFS's of the desired structure. We have an unknown in the right hand side however; we need to find the weight. We do know both $\boldsymbol{y}$ and $\boldsymbol{\phi}$ for the training set however. So we can write a different form of equation 13:

$$\boldsymbol{Y} = \boldsymbol{\Phi}\boldsymbol{w}, \tag{14}$$

where $\boldsymbol{Y}$ and $\boldsymbol{\Phi}$ contain the same information as their lowercase counterpart, but now for the reference structures. So $\boldsymbol{Y}$ contains the first principle energies, and $\boldsymbol{\Phi}$ is a collection of all $\boldsymbol{\phi}$ for all training structures. Since we know both $\boldsymbol{Y}$ and $\boldsymbol{\Phi}$, we can use these to calculate the weights and uncertainty for the EFS using the Bayesian theorem [5]:

$$\mathbf{w} = \left[\mathbf{I}/\sigma_w^2 + \boldsymbol{\Phi}^T\boldsymbol{\Phi}/\sigma_v^2\right]^{-1} \boldsymbol{\Phi}^T\mathbf{Y}/\sigma_v^2, \tag{15}$$

$$\boldsymbol{\sigma} = \sigma_v^2\mathbf{I} + \boldsymbol{\phi}^T\left[\mathbf{I}/\sigma_w^2 + \boldsymbol{\Phi}^T\boldsymbol{\Phi}/\sigma_v^2\right]^{-1} \boldsymbol{\phi}. \tag{16}$$

In these equations, $\boldsymbol{I}$ denotes the identity matrix, and $\sigma_w^2$ and $\sigma_v^2$ denote parameters which are determined such that the robustness and accuracy are balanced. The diagonal elements of $\boldsymbol{\sigma}$, which correspond to the variances of the prediction, are used as uncertainty in the prediction.

This concludes the machine learning force field method. In the next section, we shall explain how we obtain the reference structures; this is done on-the-fly.

# 3 Method

## 3.1 On-the-fly Machine learning force fields

The machine learning method VASP uses to calculate forces and energies are so called on-the-fly machine learning force fields. The difference with 'normal' machine learning force fields is that instead of starting with an already existing database of atom configurations, we now start with just one. DFT calculations are then performed until the potential energy surface is sufficiently sampled around the propagated configuration. When this happens, forces and energies are instead calculated using the force field generated by the machine learning method. If during the MD run a 'new' configuration occurs which has not been sampled enough yet, another DFT calculation is performed. This cycle of DFT and force field steps is repeated until the MD run has ended. The algorithm can be summarised as follows:

1. The machine predicts the energy, forces and stress tensor and their uncertainties for a given structure using the existing force field. If no force field is yet present, a first principle (FP) step is done.

2. The machine decides whether to do a first principles calculation (go to step 3) or a force field step (go to step 5) based on the uncertainty.

3. Perform a first principle calculation. This calculation can be added to the database to improve the force field.

4. If there are a certain amount of structures added through step 3 or the uncertainty has become to high, the force field gets improved by learning from the new structures.

5. The atomic positions and velocities are updated by using either the force field or the first principle calculation, depending on the accuracy of the force field.

6. If the requested amount of MD steps have been achieved, the program is done. If not, go back to 1.

A graphical representation of the algorithm is show in figure 4

## 3.2 VASP

To run the molecular dynamics simulations, the Vienna Ab initio Simulation Package, or VASP has been used. Within this program, the potential energy, the forces on the atoms and the stress tensor of the crystal structure are calculated based on Density Functional Theory (DFT). This thesis does not cover the detailed working of this theory, but treats the resulting data as a given database. However, multiple settings of great importance must be chosen to obtain accurate results, or even results at all. This section will be dedicated to this topic.

### 3.2.1 General VASP settings

The simulations were performed using the exchange-correlation functional in the Perdew-Burke-Ernzerhof (PBE) form. The cutoff energy ENCUT was set to 310 eV. This was chosen in accordance with max energy ENMAX of the POTCAR file, where ENCUT = 1.2ENMAX was chosen. A more generally used formula is ENCUT = 1.3ENMAX, but a prefactor of 1.2 has been chosen to speed up the calculations, without limiting the

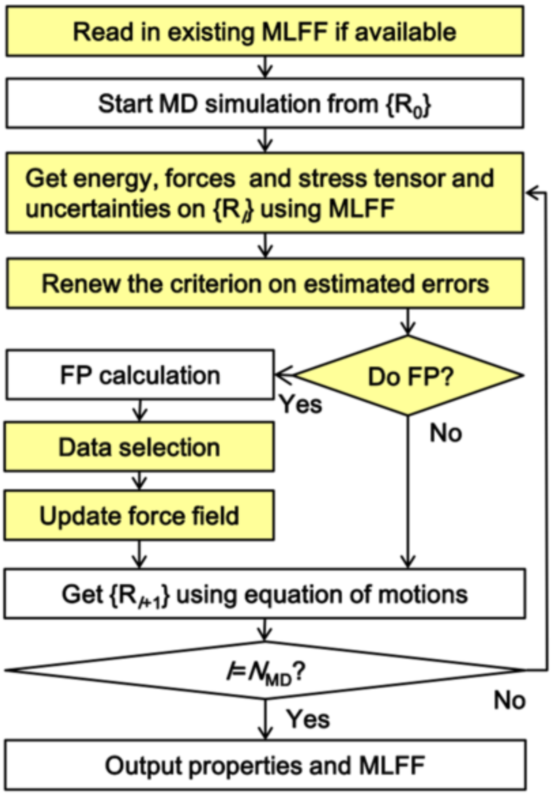
Read in existing MLFF if available
Start MD simulation from {R$_0$}
Get energy, forces and stress tensor and uncertainties on {R$_I$} using MLFF
Renew the criterion on estimated errors
Do FP?
Yes
No
FP calculation
Data selection
Update force field
Get {R$_{I+1}$} using equation of motions
I=N$_{MD}$?
Yes
No
Output properties and MLFF

FIGURE 4: On-the-fly scheme used by VASP. Here $R_I$ stands for structure $I$, with $I$ being the current MD step.

accuracy too much. The IBRION flag was set to 0, which means the Verlet algorithm is used to integrate Newtons' equations of motion. The ISIF flag has also been set, which controls whether the stress tensor is calculated and which degrees of freedom are allowed to change. The degree of freedoms which can change are the positions, cell shape and cell volume. Since we want to try and witness an superionic phase transition for which (as described in ...) the cell shape and parameters change, we put the ISIF flag such that all these values are allowed to change (so ISIF = 3). The next important flag is the MDALGO flag, which sets the thermostat which is used. This in combination with some other settings determines what ensemble the run will be held in, which is important. For this research, the Langevin thermostat was used (MDALGO = 3). In combination with the afor mentioned flags (especially the ISIF flag), this produces an NpT simulation, which is desired since we want the cell volume to be able to change while keeping the temperature as constant as possible. So ALL runs have been done in an NpT ensemble. The next important setting that has been set is the `LATTICE_CONSTRAINTS`. This parameter controls which lattice parameters are allowed to change. All three lattice parameters have been set to be able to change, since the changing of the lattice parameters is inherent for the phase transition of the material. The next flag that is very important is the POTIM flag. This parameter sets the time step between MD steps. This time step has been chosen as 2 fs, since literature doing similar simulations have also used this timestep [11]. It is furthermore able to capture nearly most vibrational frequencies in the system.

There are some other important flags, such as the machine learning flags, starting/final temperature, amount of MD steps, etc. These are however not generally the same for all runs and will hence be provided by the respective figure/section.

### 3.2.2 Training of the force field

Lets first go over the settings used to train the force field. One of the settings which has been set manually is the radial cutoff distance. This was set to a distance of 10Å, since the distance from one potassium layer to another is about 9Å. Setting this to 10Åallows the layers to 'communicate' which each other, which helps the silver layer stay in between the selenium layers. The other machine learning settings are kept standard. The training of the force field was done as follows. Firstly the force field was trained from scratch for 200 ps at 800K. This run was started with the low-temperature beta structure, converted to a a 1 ×2×3 supercell. This was done to make the force field learn the phase transition, as the DFT calculation forces the phase transition from which the force field learns. This cell was also made 3 high on purpose since, as we can see from figure 2, to have a better chance at finding the phase transition we need to make the supercell high enough such that it can stretch into the lengthy alpha phase.

The second training run started with the force field of the 800K run. This run was performed with 300K, also over 200 ps, to obtain data on the low-conductivity phase. This run also started with the low-temperature beta structure, with the same 1 × 2 × 3 supercell. This was done to get data on the $\beta$-phase.

The first principle calculations for both runs were done on a 2×3×1 regular k-grid. With these two training runs, the force field should have both high and low temperature structures, while also having seen the phase transition.

### 3.2.3 Continuous heating

To verify whether the force field can get to the experimental superionic phase, a continuous heating run was done. This run was started from the low temperature structure, in a 3×2 ×3 supercell (see figure 5). This run was done using only force field steps, to see whether the transition can be made. The run was divided in two steps; first, 400 ps at a temperature of 600K, and after this run a continuation was done for about 300 ps at 700K. The time step for both these runs was 2 fs.

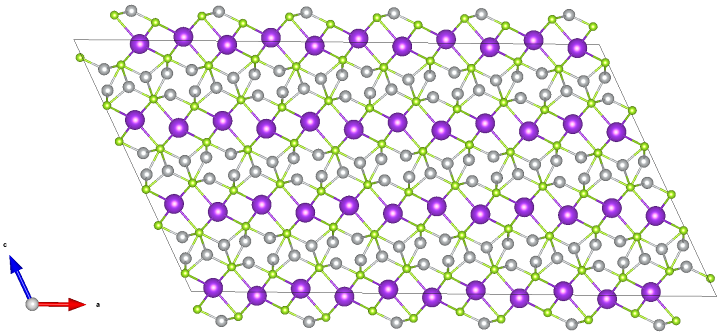

FIGURE 5: $\beta$-structure as a 3×2×3 supercell. The purple balls are potassium ions, the green balls are selenium ions and the grey balls are silver ions.

### 3.2.4 Heating

For the main result, constant temperature runs were done on temperatures ranging from 300K to 800K, with steps of 25K between each MD run. Only the fully trained force field was used for calculations, so no FP calculations. The runs were done one a 1×2×3 supercell. For each run, 55 ps was simulated with a 2 fs time step at constant temperature. Each run started from the final structure of the previous run, such that the equilibration time was little and the heating was not too sudden. After each run, the first 5 ps was taken to be equilibration time and hence removed from the data. This resulted in 50 ps per temperature from which the results were generated.

### 3.2.5 Alpha-phase

One MD run has been performed starting at the $\alpha$-phase. This run follows the exact procedure as in Rettie et al [11], except that we let the force field train and help when the uncertainty in the prediction is small enough. The simulation is 55 ps using a time step of 2 fs. In the $\alpha$-phase, the silver ions have 75% occupancy. This means that we have to remove three silver atoms from the primitive unit cell. The paper we are copying from does this at random, but we do this by removing one silver atom systematically from each layer, and then taking the configuration which has the lowest energy. After this selection, the cell was multiplied into a 4×4×1 supercell. For the FP calculations, a gamma-only k-point grid was used. This run was then performed at a constant temperature of 800K.

## 3.3 Diffusion coefficient calculation

The diffusion coefficient is a measurem of how much an atom moves . It is thus a quantity of great interest for us, as it gives information about the superionic phase transition. In this section the procedure of how the diffusion coefficient is obtained shall be given.

Before we get to the diffusion coefficient, it is important to introduce the mean squared displacement, or MSD first. The MSD is a measurement of the displacement from some predefined starting position. It is given in formula form by:

$$\mathrm{MSD}(t) = \frac{1}{N}\sum_{i=1}^{N}\frac{1}{N_t}\sum_{k=0}^{N_t}|\mathbf{r}_i(t+k\Delta t)-\mathbf{r}_i(k\Delta t)|^2, \tag{17}$$

where $N$ is the amount of atoms of the type which is being looked at. The position vector atom $i$ at time $t$ is given by $\mathbf{r}_i(t)$. $\Delta t$ is the time step used in the MD run. The second sum in equation 17 is an ensemble average over time. The idea is that the whole MD run is split in overlapping parts of size $t$. Starting from the first atomic positions, we then calculate the MSD from this location until time $t$. We then shift our starting structure one time step $\Delta t$ further, and then look at the MSD until a time $t + \Delta t$. In general, we calculate the mean squared displacement from $k\Delta t$ until $t + k\Delta t$, with $k = 0$ until $k = N_t$, where $N_t$ is the amount of pieces which fit in the total simulation time. So for a certain $t$ and $\Delta t$, only a certain amount of overlapping pieces $N_t$ can fit in the whole run. The reason this is done is because there is no reason for the first structure to be the best structure to start from. By averaging in this way, we get a more accurate value for $D$, since this procedure will result in a smoother MSD vs $t$ graph.

In in case of a random walk, the dependence of MSD vs $t$ is linear. The relation is given by the Einstein relation:

$$\mathrm{MSD}(t) = 2dDt, \tag{18}$$

where $d$ is the dimension of the diffusion and $D$ is the diffusion coefficient. In this research, even though the diffusion in the $z$-direction is small, it is still taken into account. Hence we take $d = 3$. We can thus obtain the diffusion coefficient from MSD data, which in turn can be obtained from the positions of the atoms over the MD run. There is another subtlety in calculating the diffusion coefficient however. Since we divided the MD run into multiple smaller MD runs, we calculate the diffusion coefficient over all the runs. These are then averaged over $N_t$ to obtain the desired result: the diffusion coefficient.

### 3.3.1 Error on the diffusion coefficient

Now that we have obtained a way to calculate the diffusion coefficient, we also would like to know the error on this value. We could take the standard deviation of all the diffusion coefficients calculated over the split runs. This however does not take into account the fact that at lower temperatures, less diffusion happens. Since all parts of the MSD run will look similar, independent of the temperature, the standard deviation of the mean of $D$ will grow similarly to $D$ itself. We would however like to take into consideration the fact that at lower temperatures less diffusion happens, which results in an inherently less accurate value of $D$ since we have less diffusion events. We thus adopt the method of calculating the standard deviation developed by He et al [8]. According to this method, the standard deviation is given by:

$$\sigma = D_{true} \left( \frac{A}{\sqrt{N_{eff}}} + B \right), \tag{19}$$

where $D_{true}$ is the 'true' value of the diffusivity calculated over the whole (so uncut) MD run, and $A$ $B$ are fitting constants. These values have been fitted for many superionic materials, and this resulted in values of 3.43 and 0.04 for $A$ and $B$ respectively. Since they have been fitted specifically for superionic materials, we will be using these values as well. Furthermore, $N_{eff}$ is the effective amount of ion hops which contributed to the total MSD, calculated by:

$$N_{eff} = \frac{\max_t \left[ \text{TMSD}(t) \right]}{a^2}, \tag{20}$$

where TMSD $= N \cdot$ MSD is the total mean squared displacement of all ions, and $a$ is the distance between two neighbouring Ag sites. So $\max_t \left[ \text{TMSD}(t) \right]$ is the maximum total mean squared displacement, taken over the whole MD run. Since ion hopping is the main diffusion mechanism in superionic conductors, it makes sense to relate the amount of hopping to the error in the diffusivity; more hopping means a better sampling size for the diffusion coefficient, and vice versa. Equation 19 is used to calculate the error on $D$.

## 3.4 The Activation energy

As described before, multiple runs at different, constant temperatures have been done. An diffusion coefficient can be obtained for all of these runs. These diffusion coefficients are related to the temperature $T$ by the so called Arrhenius relation by [8]:

$$D = D_0 \exp \left( \frac{-E_a}{k_b T} \right), \tag{21}$$

where $D_0$ is a model-dependent prefactor, $k_b$ the Boltzmann constant and $E_a$ the activation energy. This activation energy is an important quantity of SIC's; it tells something about how easily the atom comes 'loose' of the site, and hence how easily it starts hopping. So by fitting the logarithm of $D$ vs the inverse of $T$, a linear relation should be obtained with which the activation energy $E_a$ can be obtained:

$$\log D = \log D_0 - \frac{E_a}{k_b}\frac{1}{T} \tag{22}$$

One should be careful about the range of $T$ over which this is fitted however. The Arrhenius relation assumes that the mechanism of diffusion is the same over the fitted range of $T$. For SIC's, this means that this relation should only be fitted in the superionic region. Furthermore, the inverse of the standard deviation $\sigma$ squared should be used as weights for fitting. This is because we should weight values of $D$ which we are more certain off heavier than values we have lower statistics on.

# 4 Results and Discussion

## 4.1 Continuous heating

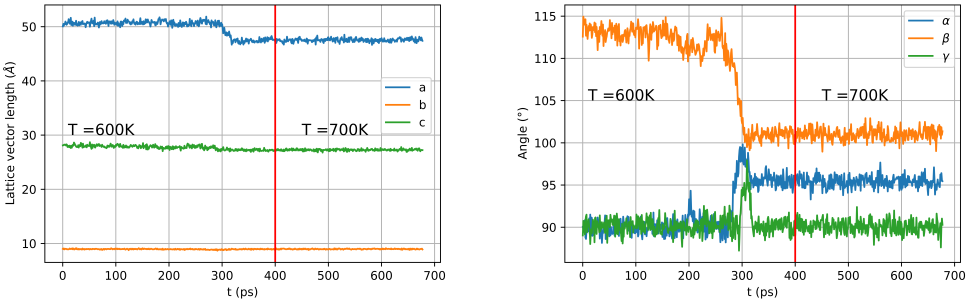

(A)

(B)

Figure 6: (A) Lattice vector length and (B) Angle change versus simulation time. These runs have been done according as described in section 3.2.3. On the left of the red line, the temperature was kept at 600K while on the right of the red line the temperature was increased to 700K.

Figure 6 shows the results from the continuous heating run as described in section 3.2.3. We can see that in the 600K regime, we observe a phase transition around 275 ps in both graphs. We can see from the values of for example the angles that this is not the 'correct' phase transition; if we compare these values to the values in table 1, we observe that only the value of $\gamma$ is the same. So even though we do observe a phase transition, we do not get to the $\alpha$-phase as observed in experiment. This could have multiple reasons as to why. One of them is that the heating was done very suddenly. We started from the 300K structure, and suddenly heated it up to 600K. It could be that the structure got broken, and the force field could not recover from this. It is more likely however that we got into some other energy minimum, since the structure does not seem broken (see figure 7. This is also supported by the fact that after we heat it to 700K, the structure still does not change, indicating we have found some other weird energy minimum. Another reason could be that the force field did not acquire correct data on the phase transition. This will be discussed in more detail in a later section. The next result shall show that eventhough we did not get to the correct $\alpha$-phase, we still observe an superionic phase transition.

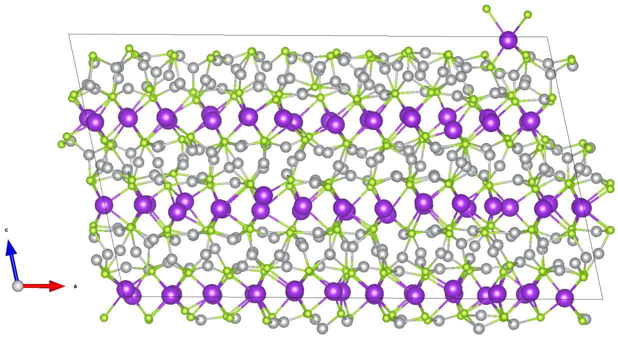

Figure 7: Final structure after continuously heating at 600K and 700K.

## 4.2 Heating

The following subsections shows the results from the heating simulations as described in section 3.2.4.

### 4.2.1 Radial distribution function

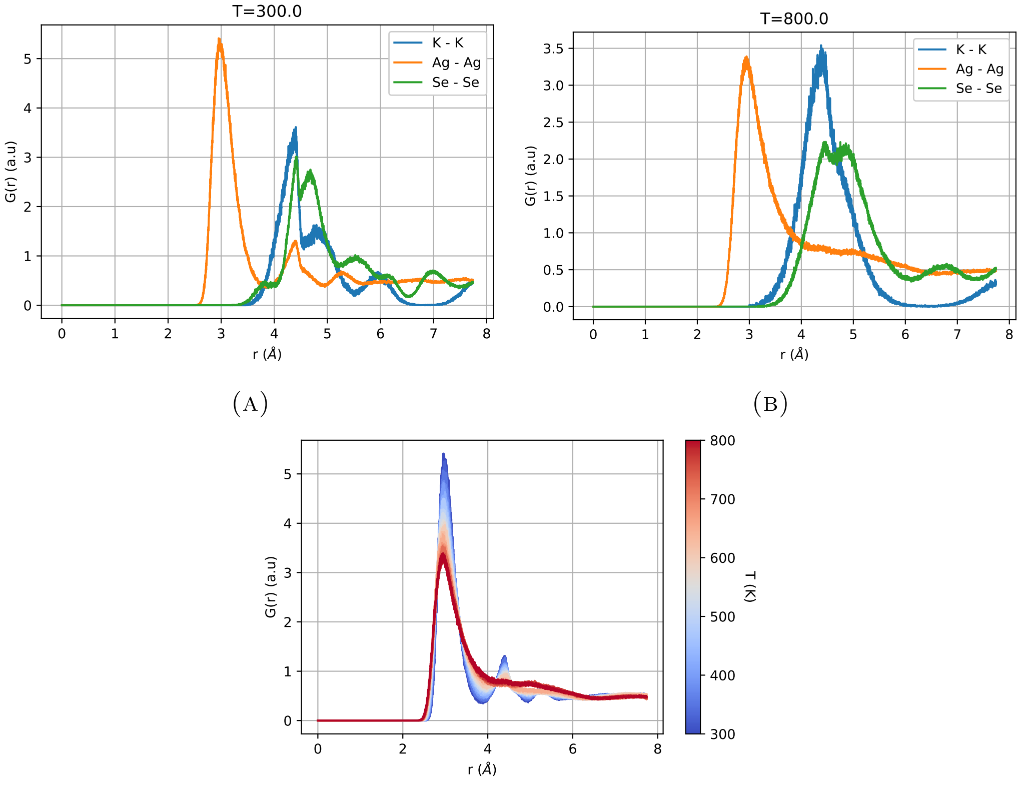

(A)

(B)

(C)

Figure 8: Results from radial distribution function calculations. (A) Radial distribution function for different atom-atom pairs for $T = 300$K. (B) Radial distribution function for different atom-atom pairs for $T = 800$K. (C) Radial distribution function for Ag-Ag pairs over different temperatures, shown in a heat map.

Figure 8 shows the radial distribution plotted against distance, for different temperatures of the heating runs (see section 3.2.4). From figure 8a we can see that at low temperatures, the RDF of all atom types show multiple peaks. This indicates that at these temperatures, there was still quite some structure in the system for all atoms, which means the system behaved solid like. From figure 8b, when we are at higher temperatures we can see that the RDF for silver has changed dramatically; the two peaks at around $r = 4.4$ Åand $r = 5.5$ Åare gone, and the graph seems to go to a constant value for higher $r$. This is very typical of a liquid; one sharp spike, and then a flat constant line. The disappearing of the secondary peaks is shown in figure 8c. We can clearly see that as $T$ increases, the silver layers start to lose structure and behave like a liquid. As for the other atom types, we can see some change here as well. It seems that both K and Se lose some structure as well, but this is too be expected as we are close to the melting point of 900K. These two atom types have a lot more structure than the silver structure though, which is to be expected since they should be keeping the silver atoms in the superionic phase.

We can furthermore see that the potassium ions are most structured at this temperature, even going to zero after the peak. From these graphs, we can conclude that we can definitely observe a superionic phase transition; the Ag layer starts to behave like a liquid for increasing temperature, while the K and Se layers still behave solid like.

### 4.2.2 Mean squared displacement

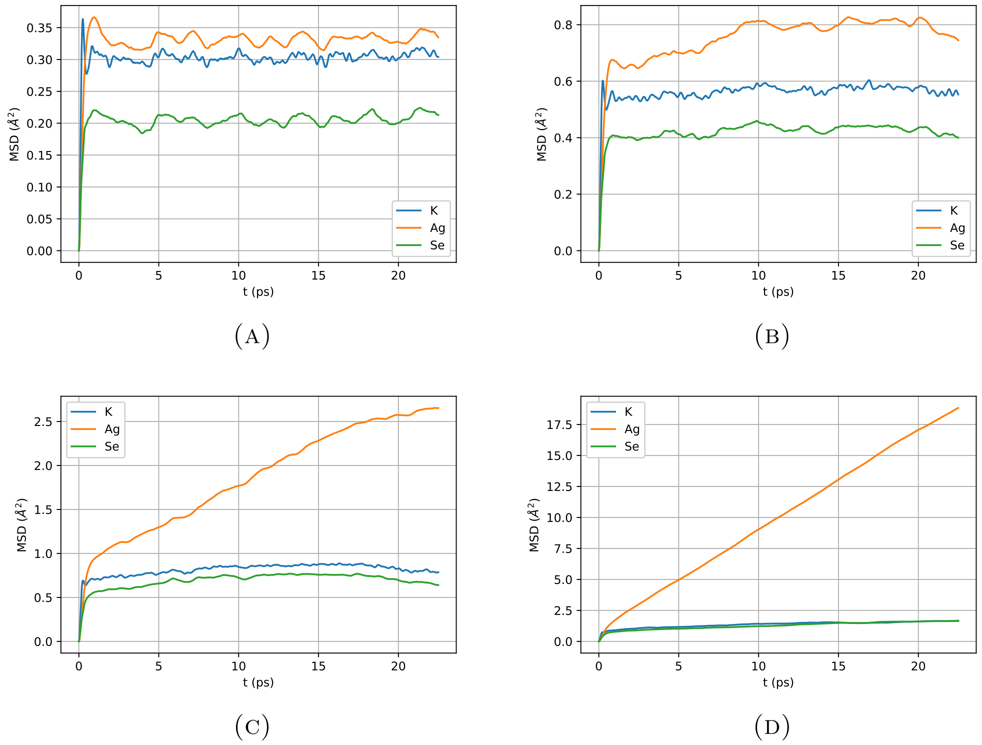

(A)

(B)

(C)

(D)

Figure 9: Graphs showing the MSD of all atom types versus time, for different temperatures. These have been averaged over the whole MD run according to equation 17. The temperatures are as following: (A) $T = 300$K, (B) $T = 500$K, (C) $T = 600$K, (D) $T = 800$K.

Figure 9 shows the MSD vs time for different temperatures. We can see that the maximal MSD increases with increasing temperature for all atom types, but by far mostly for the silver atoms. This is to be expected, since the silver layer is the mobile layer while the others should be immobile. They of course start moving a bit more, but this is inevitable since we are increasing the temperature. Another result is the clear difference between the 300K graph and the 800K graph; not only did the shape of the Ag curve change completely, the difference with the other atom types also increases sharply. From this it can be seen that we indeed have a superionic conductor; one conducting layer, with the other layers being immobile.

Figure 10 shows the MSD in all three directions vs time, for 800K. From this graph we can see that the diffusion in the x and y direction are almost identical, while the diffusion in the z direction is almost three times as low. We can clearly see the 2D element of the system from this. We do however have some diffusivity in the z direction, which is still quite some. This can be explained by the path the silver atoms take when hopping. Sometimes, even though the distance is a bit bigger than the nearest site, a silver atom

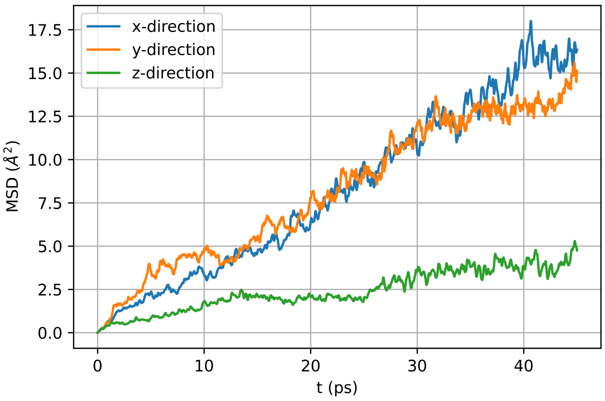

FIGURE 10: Graph of MSD vs tau for silver atoms in x,y,z direction to show 2D behaviour. This data was taken from the *whole* 800K heating run for clearity.

can hop to a site below it. This results in a mean squared displacement in the z direction, which is what we see. But is clear that most hopping happens in the x-y plane.

### 4.2.3 Diffusion

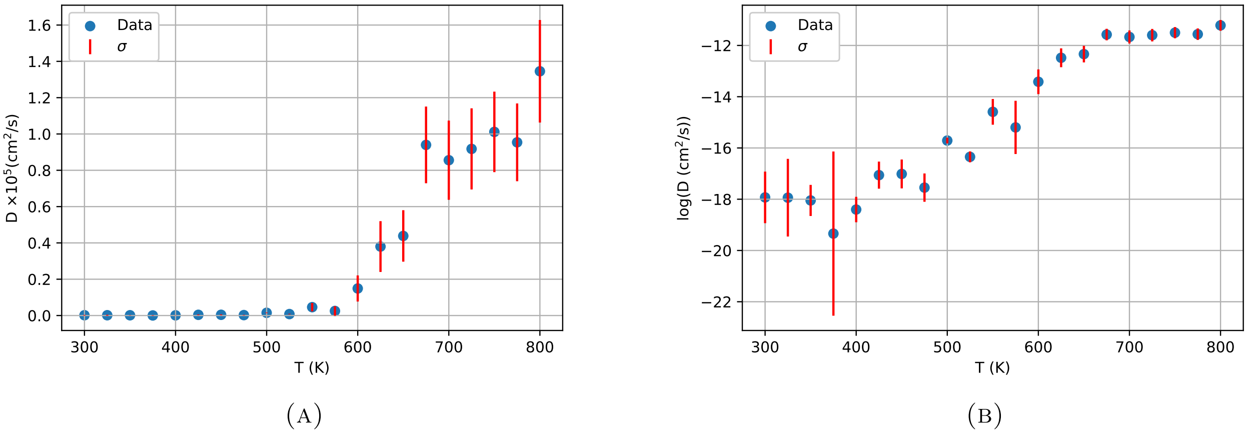

FIGURE 11: Graphs (A) Diffusion coefficient and (B) the natural logarithm of the diffusion coefficient versus temperature. The diffusion coefficients are obtained as described in section 3.3, with $\sigma$ the standard deviation from equation 19.

Figure 11 shows the diffusion coefficient plotted versus temperature, as obtained from the procedure explained in section 3.3. From figure 11a we can see something remarkable instantly; after $T = 575$K we can see a very sharp spike in diffusion coefficient, going up in orders of magnitude. This appoint this to the superionic phase transition as described in the previous section. Another striking characteristic of this graph is that the error seems to grow with temperature. This is not something which is expected, since we should have more diffusion events for larger temperatures, hence more certainty in diffusion coefficient. This is however just misleading in the plot; the errors for low temperature are actually relatively high, almost of the same order as the value of $D$ itself. In figure 11b, where the logarithm of $D$ is plotted against $T$, we can see a better representation of the relative error per point. We can see that overall, the error decreases as $T$ increases, as we would expect.

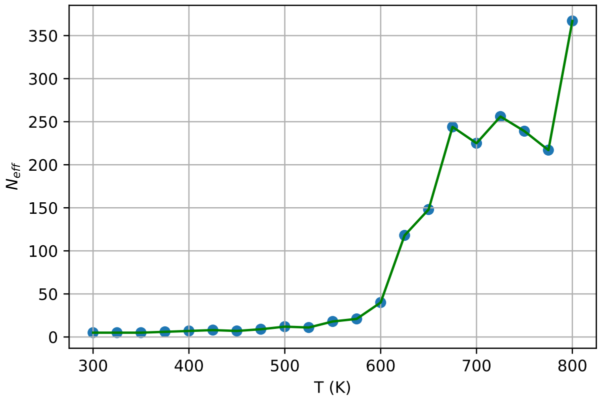

FIGURE 12: The effective number of silver hops vs temperature.

Another graph supporting the existence of the superionic phase transition can be seen in figure 12. This graph shows the effective amount of ion hops versus temperature. From this graph we can see a very similar structure as in figure 11a. We can again see a very sharp increase around $T = 575$K. This is also expected, since at low temperature we expect little to no hops as this is the low-conductivity phase. As $T$ increases, we would expect to see an increase in ion hops as we get to the superionic phase, which is what we see.

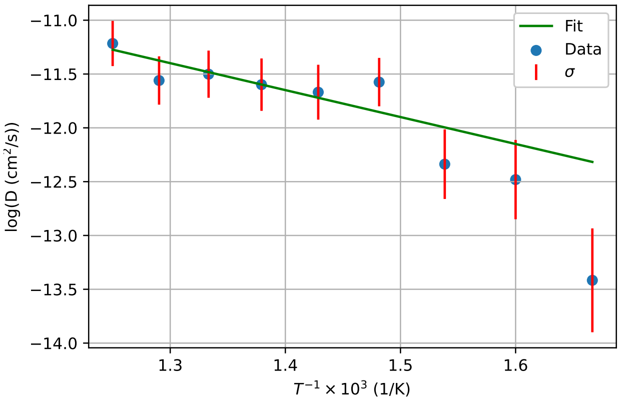

FIGURE 13: The logarithm of $D$ plotted vs the inverse of $T$ and the accompanying fit used to obtain $E_a$ for $T$ between 600 K and 800 K, which we assume corresponds to the superionic region as predicted by figure 11. The inverse of $\sigma$ squared has been used as weights for the fit.

Figure 13 shows the superionic region for which the Arrhenius relation has been fitted. The values of $\log D$ were plotted against the inverse of $T$, to then fit this relation to equation 22. In this fit, the inverse of the variance has been used as weights. This results in the diffusion coefficients which we are more certain about impact the fitting more than point we are not so certain about. For this plot, it was assumed that the superionic conduction starts happening from 600K. This is on the basis of figure 11. This results in the fit shown in the figure. From the slope of this fit, after multiplying by $-k_b$, we obtain a value of $E_a = 0.21 \pm 0.06$ eV. This is of the order of $k_bT$, which is typical for SIC's. Values for the activation energy of 0.12 eV were reported for this material [11], so we are on the same order. The reported value is not within our error region however. There are possibilities why this is the case.

## 4.3 Alpha-phase

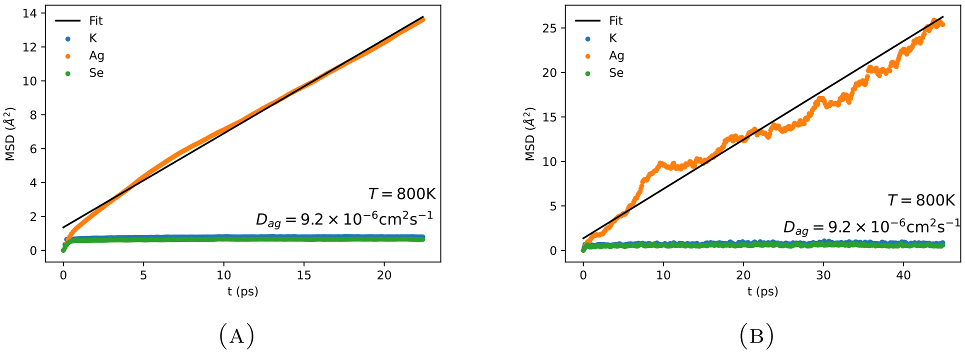

FIGURE 14: Graphs showing the MSD plotted against simulation time. The data was obtained following the procedure described in section 3.2.5. (A) Plot and fit of the diffusion coefficient for the split MD run, as can be seen by the smoothness of the graph and the length on the x-axis. (B) Plot of the *whole* MSD run versus time. The diffusion coefficient obtained from (A) has been used here to obtain the straight black line.

Figure 14 shows the result from the constant temperature run, where we start from the 'correct' $\alpha$-phase (see figure 2). We can see that the shape of the graphs are very similar to those of figure 9. This supports that our superionic phase is in fact a superionic phase, similar to that of the correct alpha phase. The values on the y-axis of 14a are also similar to the values in 9. This shows that our version of the superionic phase is somehow similar in diffusion of silver ions as the correct version. We also find the diffusion coefficient at this temperature to be $D_{ag} = 9.2 \times 10^{-6}$cm$^2$s$^{-1}$. This is in great agreement with the value of $D_{ag} = 9.9 \times 10^{-6}$cm$^2$s$^{-1}$ which Rettie et al [11] found, which shows that the help of force fields does not worsen the accuracy of the diffusion coefficient.

One thing that should be noted, but is definitely not trivial, is the time this run took. We did the exact same as Rettie et al[11], the only difference being that we let MLFF help whenever the force field was accurate enough. An average FP step took about 171 s (on 4 cores, each core having 32 cpus), while a force field step took only 0.27 s with the same computing power. This is about 629 times faster! So this run of 55 ps would have taken them about 54 days, while doing this run with only a (fully trained) force field would have only taken about two hours. This is a huge speed increase, and can save researchers tons of time/allow for bigger research.

## 4.4 The Force field

### 4.4.1 Database

After the full training was completed (as discussed in section 3.2.2), about 751 structures were in the training database. VASP predicts using the force field and calculates the

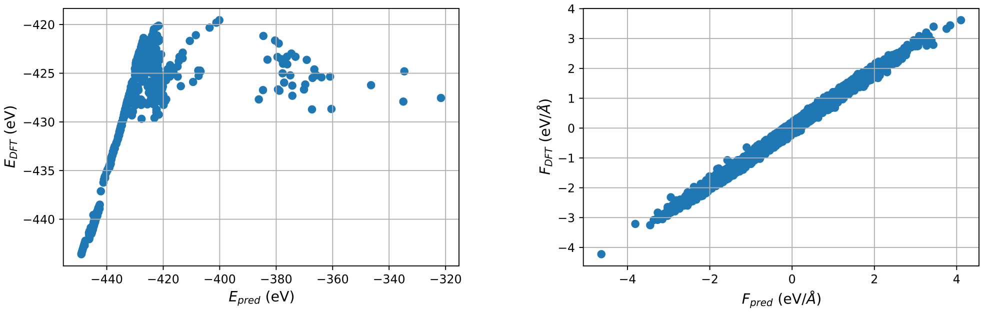

(A)

(B)

FIGURE 15: FP calculation of (A) energy and (B) forces versus the prediction of the force field on energy and forces respectively. These predictions were done on the structures in the database after the whole training of the force field was completed.

energies on the force field database, which is shown in figure 15. These are the data points which are used in equation 15 to obtain the weights. We expect to see a straight line here, since we are doing regression. We observe something strange immediately however; there are some significant outliers in the energy prediction of the database. This means that we most likely have some faulty structures in our database. The structure with the biggest outlier in energy is shown in figure 16. We can indeed see something strange happen; the silver ions are infiltrating into the selenium layers and at some places even in the potassium layers. This means that this structure is probably broken. This is most likely due to the 'harsh' training; the 300K structure was heated directly to 800K, which was most likely too big of a step and broke some of the structures. The deviating points are small in number however, so since the bulk of the points lie on a straight line the weights should still be estimated quite well.

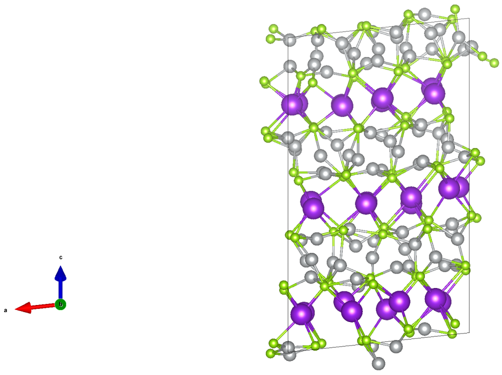

FIGURE 16: Structure from the database of the force field with the highest deviation of prediction of the energy from the bulk of the structures. The purple balls are potassium ions, the green balls are selenium ions and the grey balls are silver ions.

Curiously though, the prediction in the forces show no such deviations; all points lie on a nice straight line. This means that although we have some bad structures in our database, our force prediction is still good and hence the propagation of the system should still be quite good. Hence we can still rely on our diffusion results, even with the faulty structures in our database.

### 4.4.2 Accuracy of the force field

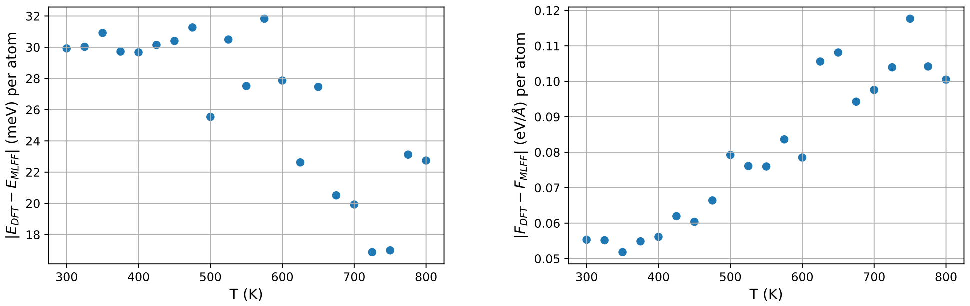

(A)

(B)

Figure 17: Plots showing the difference in (A) energy and (B) force between a DFT calculation and MLFF calculation on the same structure. From each temperature in the heating run, one random structure has been picked as structure.

Figure 17 shows the difference between the FP and a force field calculation on the same structure. One random structure was taken from each temperature of the heating run. We assume the FP calculation to be more accurate, as with MLFF we cannot become more accurate than what we have learned on as we are always approximating. The difference in values between the two methods can then be seen as the error of the MLFF method. We first observe that the error for both the energies and forces are within reasonable bounds; under 32 meV per atom and under 0.12 (eV/Å) per atom, respectively. We do observe contradicting behaviour between the energy and force trends however; the error in the energies decrease with increasing temperature, while the error increases for the forces. A possible explanation for this could be that the system stabilizes at higher temperature (since the phase transition happened), which is why the energy becomes more accurate. On the other hand, the force becomes more inaccurate because the whole system (especially the silver atoms) start having higher kinetic energies, which makes it more difficult to predict the forces. Overall however, the errors are within reasonable range.

# 5 Conclusion

Our results show that machine learning force fields are capable of describing superionic phase transitions. Eventhough diffusion becomes rapid, by choosing the VASP parameters wisely one can still get the system to be at a very reasonable size while still being accurate. While in this research, we did not get to the exact superionic phase from the low temperature phase, we did observe a superionic phase transition, with our version of the superionic phase showing good correspondence concerning diffusion. We can hence conclude that MLFF are capable of simulating thermoelectric materials with a superionic phase transition. We have also shown that if we try to exactly copy the method of another study on the same material, we can speed up the simulation with orders of magnitude while achieving nearly the same values for the diffusivity. We thus conclude that machine learning force fields can be used to significantly speed up simulations concerning SIC's. It should finally be noted that the way the force field is trained is crucial, as a dirty force field gives innacurate results. MLFF thus works, if the appropriate settings are chosen.

# 6 Outlook

One of the main letdowns of the results is that we did not get to the wanted superionic phase described in literature. This could be fixed by training the force field better. Not only did we have bad structures in our force field, but the training could have been done way more gradually instead of just on two temperatures. This would most likely get rid of the bad structures aswell. Future research could be invested in for example training in the same fashion as the heating runs; so slowly heating the material at constant temperatures, while starting the MD runs anew every temperature. This might also shift the phase transition temperature to the experimental value of 700K. Another aspects that could be further researched are the types of SIC's. In this research, we have only looked at a type I superionic conductor. But while we do not expect it, the MLFF method might not work/work better for different types of SIC's as they follow different phase transition curves. The results have shown that $KAg_3Se_2$ is a complex material. Simpler SIC's could be checked with the MLFF method too see if the experimental superionic phase can be achieved there.

## References

[1] Global emissions, Mar 2022.

[2] Albert P. Bartók, Risi Kondor, and Gábor Csányi. On representing chemical environments. Physical Review B, 87(18), 2013.

[3] Albert P. Bartók, Mike C. Payne, Risi Kondor, and Gábor Csányi. Gaussian approximation potentials: The accuracy of quantum mechanics, without the electrons. Physical Review Letters, 104(13), 2010.

[4] Qinghan Bian. Waste heat: The dominating root cause of current global warming. Environmental Systems Research, 9(1), 2020.

[5] Christopher M. Bishop. Pattern recognition and machine learning. Springer, 2016.

[6] J.B. Boyce and B.A. Huberman. Superionic conductors: Transitions, structures, dynamics. Physics Reports, 51(4):189265, 1979.

[7] Peter A. Finn, Ceyla Asker, Kening Wan, Emiliano Bilotti, Oliver Fenwick, and Christian B. Nielsen. Thermoelectric materials: Current status and future challenges, August 2021.

[8] Xingfeng He, Yizhou Zhu, Alexander Epstein, and Yifei Mo. Statistical variances of diffusional properties from ab initio molecular dynamics simulations. npj Computational Materials, 4(1), 2018.

[9] Ryosuke Jinnouchi, Ferenc Karsai, and Georg Kresse. On-the-fly machine learning force field generation: Application to melting points. Physical Review B, 100(1), 2019.

[10] Ryosuke Jinnouchi, Jonathan Lahnsteiner, Ferenc Karsai, Georg Kresse, and Menno Bokdam. Phase transitions of hybrid perovskites simulated by machine-learning force fields trained on the fly with bayesian inference. Physical Review Letters, 122(22), 2019.

[11] Alexander J. Rettie, Jingxuan Ding, Xiuquan Zhou, Michael J. Johnson, Christos D. Malliakas, Naresh C. Osti, Duck Young Chung, Raymond Osborn, Olivier Delaire, Stephan Rosenkranz, and et al. A two-dimensional type i superionic conductor. Nature Materials, 20(12):16831688, 2021.

[12] Alexander J. Rettie, Christos D. Malliakas, Antia S. Botana, James M. Hodges, Fei Han, Ruiyun Huang, Duck Young Chung, and Mercouri G. Kanatzidis. Ag2se to kag3se2: Suppressing orderdisorder transitions via reduced dimensionality. Journal of the American Chemical Society, 140(29):91939202, 2018.

[13] Ramin Rojaee and Reza Shahbazian-Yassar. Two-dimensional materials to address the lithium battery challenges. ACS Nano, 14(3):26282658, 2020.

[14] Zhe Xiao, Renheng Wang, Dongting Jiang, Zhengfang Qian, Yan Li, Kaishuai Yang, Yiling Sun, Zhiyuan Zeng, and Feixiang Wu. Recent developments of two-dimensional anode materials and their composites in lithium-ion batteries. ACS Applied Energy Materials, 4(8):74407461, 2021.